

Resonant Ultrasound Spectroscopy for Irregularly-Shaped Samples and its Application to Uranium Ditelluride

Florian Theuss,¹ Gregorio de la Fuente Simarro,¹ Avi Shragai,¹ Gael Grissonnanche,¹ Ian M Hayes,² Shanta Saha,² Tatsuya Shishidou,³ Taishi Chen,⁴ Satoru Nakatsuji,^{4,5,6,7} Sheng Ran,⁸ Michael Weinert,³ Nicholas P Butch,^{2,9} Johnpierre Paglione,² and B. J. Ramshaw^{1,*}

¹*Laboratory of Atomic and Solid State Physics, Cornell University, Ithaca, NY 14853, USA*

²*Quantum Materials Center, Department of Physics,*

University of Maryland, College Park, Maryland 20742, USA

³*Department of Physics, University of Wisconsin-Milwaukee, Milwaukee, Wisconsin 53201, USA*

⁴*The Institute for Solid State Physics, The University of Tokyo, Kashiwa, Chiba 277-8581, Japan*

⁵*Department of Physics, The University of Tokyo, Tokyo 113-0033, Japan*

⁶*Institute for Quantum Matter and Department of Physics and Astronomy,*

Johns Hopkins University, Baltimore, MD 21218, USA

⁷*Trans-scale Quantum Science Institute, University of Tokyo, Tokyo 113-0033, Japan*

⁸*Department of Physics, Washington University in St. Louis, St. Louis, MO 63130, USA*

⁹*NIST Center for Neutron Research, National Institute of Standards and Technology,*

100 Bureau Drive, Gaithersburg, Maryland 20899, USA

(Dated: March 13, 2024)

Resonant ultrasound spectroscopy (RUS) is a powerful technique for measuring the full elastic tensor of a given material in a single experiment. Previously, this technique was limited to regularly-shaped samples such as rectangular parallelepipeds, spheres, and cylinders [1]. We demonstrate a new method for determining the elastic moduli of irregularly-shaped samples, extending the applicability of RUS to a much larger set of materials. We apply this new approach to the recently-discovered unconventional superconductor UTe₂ and provide its elastic tensor at both 300 and 4 kelvin.

I. INTRODUCTION

UTe₂ is a recently-discovered unconventional superconductor [2] with large upper critical fields [2, 3] and an NMR Knight shift [4–6] that suggest spin-triplet pairing. There are, however, many unsolved mysteries in UTe₂, including field-reentrant superconductivity [7–10], time-reversal symmetry breaking [11, 12], a phase transition between superconducting ground states as a function of magnetic field [13], and the occurrence of two superconducting transitions in certain samples [12, 14–16]. Underlying many of these mysteries is the question of what is the symmetry of the superconducting order parameter in UTe₂.

Externally applied stress has proven to be a useful tuning parameter when investigating these types of questions. For example, there are two unambiguous superconducting phase transitions in UTe₂ under hydrostatic pressure [10, 17], and uniaxial pressure experiments [18] imply an insensitivity of the superconducting order parameter to shear strain. However, while stress and pressure are conceptually straightforward parameters to tune externally, the more physically-relevant quantity—related to microscopic bond distances and unit cell volumes—is strain. Stress, σ , and strain, ϵ , are linearly related through the elastic tensor, $\sigma = c\epsilon$, and converting from the experimentally-determined stress to strain requires the full elastic tensor. For example, the full elastic tensor was central in determining the quantitative relation-

ship between strain, the van Hove point, and superconductivity in Sr₂RuO₄ [19, 20], as well as the relationship between anisotropic strains and superconductivity in CeIrIn₅ [21].

The full elastic tensor of a material can be determined with resonant ultrasound spectroscopy (RUS). RUS measures the mechanical resonance spectrum of a three dimensional solid. The resonance frequencies are determined by both intrinsic sample properties—the density and elastic moduli—as well as by the sample boundary conditions. If the elastic moduli, density, and sample geometry are known, then the resonance frequencies are easily calculated numerically—the “forward problem”—either using the method of Visscher *et al.* [1] or by finite elements [22, 23]. The inverse problem—obtaining the elastic moduli from a measured resonance spectrum—is more challenging because it requires multiple numerical evaluations of the forward problem and the navigation of a complex parameter landscape with many local minima [24].

For simple geometries with easily-defined boundaries—typically rectangular parallelepipeds, cylinders, or spheres—the method of Visscher *et al.* [1] can be combined with either Levenberg-Marquardt or heuristic (such as genetic algorithm) fitting methods to solve the inverse problem and obtain the elastic moduli from the resonance spectrum. For irregular samples, however, finite elements has been traditionally used to solve the forward problem. The difficulty with this approach is that finite elements is too computationally intensive to use when solving the inverse problem. This has largely restricted the applicability of RUS to materials where

* bradramshaw@cornell.edu

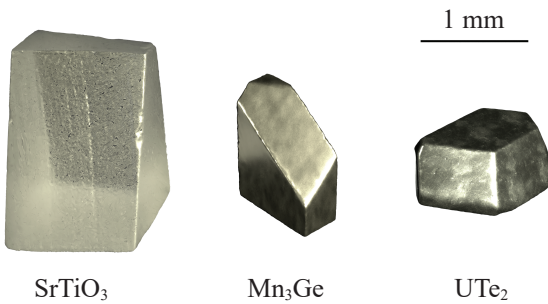


FIG. 1. CT-Scan Models. 3D models of the irregularly-shaped samples used for RUS measurements based on CT-scans. From left to right: SrTiO₃ sample B, Mn₃Ge sample B, UTe₂.

regularly-shaped samples can be prepared.

In the case of UTe₂, preparation of a rectangular parallelepiped is difficult due to the brittle nature of the material (in addition to the potential hazards associated with polishing uranium compounds). In this work, we take advantage of the recent development by Shragai *et al.* [25] that solves the forward problem for irregularly-shaped samples in a way that is two orders of magnitude faster than finite elements. This has allowed us to develop a protocol for solving the inverse problem for irregularly-shaped samples. We demonstrate this protocol on samples of SrTiO₃ and Mn₃Ge—compounds with known elastic moduli—and then apply our new technique to obtain the full elastic tensor of UTe₂ at 300 K and at 4 K.

II. METHODS

Resonant ultrasound spectroscopy. We performed RUS measurements by placing a sample in weak mechanical contact between two piezoelectric transducers, providing nearly-free boundary conditions. One transducer is driven with an AC voltage at fixed frequency, and the voltage generated on the other transducer is measured using a lockin amplifier. By stepping the drive frequency from roughly 100 kHz to 5 MHz, we obtain the first one hundred or so mechanical resonances for a typical, mm-scale sample. More details of the experimental setup and how to measure resonance spectra can be found in Ramshaw *et al.* [24] and Balakirev *et al.* [26]. Full lists of all experimental resonance spectra used in this study are given in the supplement.

Fitting resonance spectra. Resonance spectra are calculated by minimizing the linear elastic Lagrangian as a function of the displacement field $\vec{u}(\vec{r}, t)$,

$$\mathcal{L} = \frac{1}{2} \int \left(\sum_i \rho \dot{u}_i^2(\vec{r}) - \sum_{ijkl} c_{ijkl} \frac{\partial u_i(\vec{r})}{\partial r_j} \frac{\partial u_k(\vec{r})}{\partial r_l} \right) dV, \quad (1)$$

where ρ is the density, c_{ijkl} is the elastic tensor, and the

integral is over the entire volume of the sample. The widely-adopted method of Visscher *et al.* [1] expands the displacements fields in a polynomial basis and solves the volume integrals numerically. This method works well for rectangular parallelepipeds, cylinders, and spheres [26], where the boundaries are easily defined. For irregularly-shaped samples, however, this method is insufficient and new methods for computing the resonance spectra must be used.

We implement two new resonance spectra calculation methods—two “forward” solvers—into a genetic algorithm, extending the RUS fitting routine to irregularly-shaped samples. Details of the genetic algorithm itself can be found in Ramshaw *et al.* [24] and in the supplement; here we focus on incorporating and verifying the new forward solvers.

The first forward solver extends Visscher’s method to irregular samples by converting the volume integrals to surface integrals [25]. We will refer to fits performed with this forward solver as SMI (surface mesh integration [25]).

The second forward solver is a commercially-available finite element solver: Comsol. We implement a Comsol forward solver to verify the newer SMI method (note that the use of FEM to calculate the forward problem for RUS was described earlier in Liu and Maynard [22]). We will refer to fits performed using Comsol as FEM.

Both SMI and FEM-based fits are compared to fits using Visscher’s approach for rectangular parallelepiped samples. Fits with Visscher’s approach are referred to as RPR.

Sample digitization and alignment. Both the SMI and FEM methods require three-dimensional digitizations of the samples. FEM uses the full, three-dimensional tetrahedral mesh of the entire sample volume. SMI uses only the surface triangles of the same mesh (this includes any “interior” surfaces around voids). These digitizations were obtained with a Zeiss Xradia Versa XRM-520 X-ray nano-CT and are shown in Figure 1. The mesh size used for our fits depends on the solver method, as well as on the sample shape and size. We use a mesh with average linear dimension 10 μm for SMI, and 60 μm for FEM (FEM uses a larger mesh because it is much more computationally intensive than SMI). The samples are oriented to within 1 degree using Laue backreflection diffractometry. The mesh is then aligned to the crystal axes by identifying two flat faces on the sample which uniquely relate the surface mesh to the orientation of the sample in the Laue apparatus. More details on sample digitization can be found in the SI.

Measurement uncertainty. The uncertainties in our fits have two dominant contributions. One contribution originates from small deviations from the weak-coupling approximation: the resonance frequencies depending weakly on how the sample is mounted in the apparatus. This is predominantly due to the finite force exerted on the sample by the weight of the cantilever holding the top ultrasonic transducer. By remounting the samples in different orientations in our RUS apparatus, we find uncertainties in the elastic moduli of approx-

imately 2 GPa for the SrTiO₃ and Mn₃Ge samples, and 0.5 GPa for UTe₂. The second largest source of uncertainty is due to uncertainty in the alignment between the crystal axes and the sample mesh. This uncertainty is approximately 1 degree around each axis and results in uncertainties of typically 0.03 GPa for all regularly-shaped samples. This uncertainty is larger for all irregularly-shaped samples—on average 0.4 GPa, 2 GPa, 0.5 GPa for the irregular SrTiO₃, Mn₃Ge, and UTe₂ samples, respectively. A detailed error analysis can be found in the SI.

Density functional theory calculations. We used density-functional theory to produce estimates of the elastic moduli of UTe₂. This involved total energy calculations following the procedure of Ravindran et al. [27]. The full-potential linearized augmented plane wave method [28] calculations employed the generalized gradient approximation [29] for the exchange correlation, wave function and potential energy cutoffs of 16 and 200 Ry, respectively, muffin-tin sphere radii of 1.35 Å, and an $8 \times 8 \times 8$ k -point mesh. Spin-orbit coupling was fully taken into account in the assumed nonmagnetic state. The elastic tensor was extracted from fits of the total energy variations around the experimental structure [30] to the energy-strain formula [27], including linear terms. The resulting moduli are given in Table III.

III. TEST RESULTS

We test the implementation of two forward solvers—FEM and SMI—for fitting the RUS spectra of irregularly-shaped samples using a genetic algorithm. We compare these results to the moduli extracted for rectangular parallelepiped samples that can be fit using the RPR forward solver, in addition to the FEM and SMI methods. We find agreement between all methods and all sample geometries to within our measurement uncertainties. It's worth noting that while both FEM and SMI are capable of fitting RUS spectra from irregularly-shaped samples, the SMI method is two orders of magnitude faster than FEM, taking under an hour to produce a fit while FEM takes several days or even weeks.

SrTiO₃. Our first test system for our new fitting method is SrTiO₃, whose elastic tensor consists of only three independent elements due to its cubic crystal structure (point group O_h). RUS measurements and fits are performed on two samples (Table I): Sample A is polished into a rectangular parallelepiped with dimensions $(1.49 \times 2.035 \times 3.02)$ mm³, with edges oriented along the crystallographic axes. We can perform fits using all three methods—RPR, SMI, and FEM—in this simple geometry. Sample B was prepared with an irregular shape (see Figure 1 for a 3D model based on a CT scan). Only SMI and FEM fits are possible for this geometry.

The fit results are shown in Table I. Comparing the fits within each sample, we see that all methods yield identical results within uncertainties (± 2 GPa). This demonstrates that, given the same experimental data

Sample	Fit Method	c_{11}	c_{12}	c_{44}
SrTiO ₃ A	RPR	322	104	125
	FEM	322	104	125
	SMI	322	104	125
SrTiO ₃ B	FEM	317	103	122
	SMI	317	103	122
Bell et al. [31]		317.3	102.3	123.4
Poindexter et al. [32]		348.2	100.6	119.0

TABLE I. **Elastic moduli of SrTiO₃.** The elastic moduli in GPa for both SrTiO₃ samples: the sample polished into the shape of a rectangular parallelepiped (Sample A), and the irregularly-shaped sample (Sample B). Uncertainties are approximately ± 2 GPa (due to the finite force applied to the sample by the RUS apparatus) and ± 0.4 GPa (from up to 1 degree misalignment between the crystal axes and the sample mesh). Literature values are provided for comparison.

and sample geometry, all three forward solvers used in a genetic algorithm yield the same elastic moduli. This is consistent with previous demonstrations that the three methods of forward computation—RPR, SMI, and FEM—are consistent to better than 1 part in 10^4 [25].

We observe differences of less than 2.5 % for all elastic moduli when comparing the rectangular parallelepiped (sample A) and irregular (sample B) samples. These difference are on the order of our estimated uncertainties due to sample loading; alternatively, these deviations could be attributed to systematic uncertainties in the RUS measurement process such as deviations from a perfect rectangular parallelepiped for sample A, or sample imperfections that were not captured by the CT scan such as small voids or inclusions. Within our uncertainty, all of our fits are compatible with the measurements of Bell and Rupprecht [31] and Poindexter and Giardini [32] (bottom rows of Table I). We therefore conclude that our new fitting methods provide reliable elastic moduli, even for samples with irregular geometries.

Mn₃Ge. Next, we test Mn₃Ge, point group D_{6h} , which has 5 independent elastic moduli. The results of the fits are given in Table II. Similar to SrTiO₃, we show fit results for a rectangular parallelepiped sample (sample A) with dimensions $(0.87 \times 1.01 \times 1.19)$ mm³ and corners parallel to high-symmetry directions, as well as an irregularly-shaped sample (sample B—see Figure 1 for a 3D model).

As with SrTiO₃, all fit methods yield the same moduli for Mn₃Ge for both samples to within measurement uncertainty. Our results for sample A are also in agreement with previously-published elastic moduli of Mn₃Ge [33]. Comparing samples A and B, the absolute difference in elastic moduli stays below 4 GPa. This value is consistent with our results for SrTiO₃ and is likely due to similar systematic uncertainties described above.

Sample	Fit Method	c_{11}	c_{12}	c_{13}	c_{33}	c_{44}
$\text{Mn}_3\text{Ge A}$	RPR	130	44	13	202	48
	FEM	130	44	13	202	48
	SMI	130	44	13	202	48
$\text{Mn}_3\text{Ge B}$	FEM	127	40	14	203	49
	SMI	127	40	14	203	49

TABLE II. **Elastic moduli of Mn_3Ge .** The elastic moduli in GPa for both Mn_3Ge samples: a rectangular parallelepiped (sample A) and the irregularly-shaped sample (sample B). Uncertainties are approximately ± 2 GPa (due to the finite force applied to the sample by the RUS apparatus) and ± 2 GPa (from up to 1 degree misalignment between the crystal axes and the sample mesh).

T (K)	c_{11}	c_{22}	c_{33}	c_{12}	c_{13}	c_{23}	c_{44}	c_{55}	c_{66}	
RUS	4	90.3	144.1	95.9	25.7	41.3	31.9	28.0	53.2	30.4
	300	84.7	139.5	91.1	26.8	38.1	31.6	26.9	52.4	29.7
DFT	96	136	90	28	46	26	28	57	31	

TABLE III. **Elastic moduli of UTe_2 .** The elastic moduli of the UTe_2 sample shown in Figure 1 at 300 K and at 4 K. Uncertainties are approximately ± 0.5 GPa (due to the finite force applied to the sample by the RUS apparatus) and ± 0.5 GPa (from a 1 degree misalignment between the crystal axes and the sample mesh). Moduli obtained from DFT calculations, with atomic coordinates optimized, are given on the bottom row. These values were used as rough guides to constrain the parameter space of the genetic algorithm fits to the RUS data.

IV. APPLICATION TO UTe_2

Having demonstrated the successful extraction of elastic moduli from RUS spectra of irregular samples, we now fit the elastic moduli for an irregularly-shaped sample of UTe_2 . A 3D model of the sample is shown in Figure 1, and the moduli are given in Table III.

UTe_2 is orthorhombic (point group D_{2h}), with nine independent elastic moduli. The population size—the number of initial guesses—required for a good fit using a genetic algorithm scales roughly linearly with the number of free parameters [34]. This means that the UTe_2 fits require nearly twice the population as compared to the previous Mn_3Ge fits. Additionally, the samples of SrTiO_3 and Mn_3Ge were produced by adding additional facets to what were previously rectangular parallelepiped samples, whereas our UTe_2 sample is as-grown. This results in smaller feature sizes on the UTe_2 sample as compared to the previous samples, requiring a finer mesh size for the 3D models (the full meshes are shown in the supplement).

Both the dense mesh of our particular sample, and large number of moduli for UTe_2 in general, increase the fit time for the FEM method, which must re-compute the entire spectrum at each stage of the fit. As noted in Shragai *et al.* [25], this makes FEM unsuitable for fitting under these circumstances, as convergence would take upward of a month. The SMI method, on the other hand, is largely unaffected by the increase in population size and mesh density because the computationally-intensive

step is performed only once, at the start of the fit, and the results are stored for use in subsequent generations of the genetic algorithm. We therefore only perform SMI fits to our UTe_2 spectra. This approach is justified by the results of the previous section, which demonstrated that fits using both FEM and SMI methods produce the same elastic moduli.

The elastic moduli of UTe_2 , at both 300 K and 4 K are given in Table III. For comparison, we also report elastic moduli obtained from density-functional theory calculations (bottom row in Table III). These calculated values are in remarkable agreement with the experimental results. Other experimentally-relevant quantities, including the bulk modulus, the Young's moduli, and the Poisson's ratios, are tabulated in the supplement.

V. CONCLUSION

We implement two new methods for performing the forward calculation for resonance spectra in a genetic algorithm. These methods—SMI and FEM—allow us to fit the elastic moduli of irregularly-shaped samples using resonant ultrasound spectroscopy. This is first demonstrated on materials with known elastic moduli (SrTiO_3 and Mn_3Ge), demonstrating consistency between our new methods and the older method of Visscher *et al.* [1], which is only applicable for rectangular parallelepipeds. We then apply our new method to measure the full elastic tensor of the unconventional superconductor UTe_2 at 300 K and at 4 K (Table III).

We expect that the elastic moduli of UTe_2 will be of use to researchers studying the superconducting properties under both uniaxial strain and hydrostatic pressure [9, 10, 15, 17, 18, 35]. We expect that the general method that we have introduced—implementing the fast surface mesh integration method into a genetic algorithm—will be broadly useful for measuring the elastic moduli of samples that cannot be easily prepared into regular geometric shapes.

VI. ACKNOWLEDGMENTS

B. J. R., F. T., G. G., and A. S. acknowledge funding from the Office of Basic Energy Sciences of the United States Department of Energy under Award No. DE-SC0020143 (UTe_2 and SrTiO_3 sample preparation, ultrasound experiments, and data analysis). B. J. R., F. T., G. G., A. S., T. C., and S. N. acknowledge funding from the Institute for Quantum Matter, an Energy Frontier Research Center funded by the Office of Basic Energy Sciences of the United States Department of Energy under Award No. DE-SC0019331 (Mn_3Ge sample growth and preparation). Imaging data was acquired through the Cornell Institute of Biotechnology's Imaging Facility, with NIH S10OD012287 for the ZEISS/Xradia Versa 520 X-ray Microscope (CT). Laue backreflection diffraction measurements made use of the Cornell Cen-

ter for Materials Research Shared Facilities which are supported through the NSF MRSEC program (DMR-1719875). Research at the University of Maryland was supported by Department of Energy under award no. DE-SC-0019154 (sample characterization), the Gordon

and Betty Moore Foundation's EPiQS Initiative through grant no. GBMF9071 (materials synthesis), NIST, and the Maryland Quantum Materials Center. Discussion of commercial software does not imply endorsement by NIST.

-
- [1] W. M. Visscher, A. Migliori, T. M. Bell, and R. A. Reinert, On the normal modes of free vibration of inhomogeneous and anisotropic elastic objects, *The Journal of the Acoustical Society of America* **90**, 2154 (1991).
- [2] S. Ran, C. Eckberg, Q.-P. Ding, Y. Furukawa, T. Metz, S. R. Saha, I.-L. Liu, M. Zic, H. Kim, J. Paglione, and N. P. Butch, Nearly ferromagnetic spin-triplet superconductivity, *Science* **365**, 684 (2019).
- [3] D. Aoki, A. Nakamura, F. Honda, D. Li, Y. Homma, Y. Shimizu, Y. J. Sato, G. Knebel, J.-P. Brison, A. Pourret, D. Braithwaite, G. Lapertot, Q. Niu, M. Vališka, H. Harima, and J. Flouquet, Unconventional Superconductivity in Heavy Fermion UTe₂, *Journal of the Physical Society of Japan* **88**, 043702 (2019).
- [4] G. Nakamine, S. Kitagawa, K. Ishida, Y. Tokunaga, H. Sakai, S. Kambe, A. Nakamura, Y. Shimizu, Y. Homma, D. Li, F. Honda, and D. Aoki, Superconducting Properties of Heavy Fermion UTe₂ Revealed by ¹²⁵Te-nuclear Magnetic Resonance, *Journal of the Physical Society of Japan* **88**, 113703 (2019).
- [5] G. Nakamine, K. Kinjo, S. Kitagawa, K. Ishida, Y. Tokunaga, H. Sakai, S. Kambe, A. Nakamura, Y. Shimizu, Y. Homma, D. Li, F. Honda, and D. Aoki, Inhomogeneous Superconducting State Probed by ¹²⁵Te NMR on UTe₂, *Journal of the Physical Society of Japan* **90**, 064709 (2021).
- [6] H. Fujibayashi, G. Nakamine, K. Kinjo, S. Kitagawa, K. Ishida, Y. Tokunaga, H. Sakai, S. Kambe, A. Nakamura, Y. Shimizu, Y. Homma, D. Li, F. Honda, and D. Aoki, Superconducting Order Parameter in UTe₂ Determined by Knight Shift Measurement, *Journal of the Physical Society of Japan* **91**, 043705 (2022).
- [7] G. Knebel, W. Knafo, A. Pourret, Q. Niu, M. Vališka, D. Braithwaite, G. Lapertot, M. Nardone, A. Zittouni, S. Mishra, I. Sheikin, G. Seyfarth, J. P. Brison, D. Aoki, and J. Flouquet, Field-Reentrant Superconductivity Close to a Metamagnetic Transition in the Heavy-Fermion Superconductor UTe₂, *Journal of the Physical Society of Japan* **88**, 063707 (2019).
- [8] S. Ran, I. L. Liu, Y. S. Eo, D. J. Campbell, P. M. Neves, W. T. Fuhrman, S. R. Saha, C. Eckberg, H. Kim, D. Graf, F. Balakirev, J. Singleton, J. Paglione, and N. P. Butch, Extreme magnetic field-boosted superconductivity, *Nature Physics* **15**, 1250 (2019).
- [9] S. Ran, H. Kim, I.-L. Liu, S. R. Saha, I. Hayes, T. Metz, Y. S. Eo, J. Paglione, and N. P. Butch, Enhancement and reentrance of spin triplet superconductivity in UTe₂ under pressure, *Physical Review B* **101**, 140503 (2020).
- [10] D. Aoki, F. Honda, G. Knebel, D. Braithwaite, A. Nakamura, D. X. Li, Y. Homma, Y. Shimizu, Y. J. Sato, J. P. Brison, and J. Flouquet, Multiple Superconducting Phases and Unusual Enhancement of the Upper Critical Field in UTe₂, *Journal of the Physical Society of Japan* **89**, 053705 (2020).
- [11] D. S. Wei, D. Saykin, O. Y. Miller, S. Ran, S. R. Saha, D. F. Agterberg, J. Schmalian, N. P. Butch, J. Paglione, and A. Kapitulnik, Interplay between magnetism and superconductivity in UTe₂, *Physical Review B* **105**, 024521 (2022).
- [12] I. M. Hayes, D. S. Wei, T. Metz, J. Zhang, Y. S. Eo, S. Ran, S. R. Saha, J. Collini, N. P. Butch, D. F. Agterberg, A. Kapitulnik, and J. Paglione, Multicomponent superconducting order parameter in UTe₂, *Science* **373**, 797 (2021).
- [13] A. Rosuel, C. Marcenat, G. Knebel, T. Klein, A. Pourret, N. Marquardt, Q. Niu, S. Rousseau, A. Demuer, G. Seyfarth, G. Lapertot, D. Aoki, D. Braithwaite, J. Flouquet, and J.-P. Brison, Field-induced tuning of the pairing state in a superconductor, *arXiv:2205.04524* (2022).
- [14] L. P. Cairns, C. R. Stevens, C. D. O'Neill, and A. Huxley, Composition dependence of the superconducting properties of UTe₂, *Journal of Physics Condensed Matter* **32**, 415602 (2020).
- [15] S. M. Thomas, C. Stevens, F. B. Santos, S. S. Fender, E. D. Bauer, F. Ronning, J. D. Thompson, A. Huxley, and P. F. S. Rosa, Spatially inhomogeneous superconductivity in UTe₂, *Physical Review B* **104**, 224501 (2021).
- [16] P. F. S. Rosa, A. Weiland, S. S. Fender, B. L. Scott, F. Ronning, J. D. Thompson, E. D. Bauer, and S. M. Thomas, Single thermodynamic transition at 2 K in superconducting UTe₂ single crystals, *Communications Materials* **3**, 33 (2022).
- [17] D. Braithwaite, M. Vališka, G. Knebel, G. Lapertot, J.-P. Brison, A. Pourret, M. E. Zhitomirsky, J. Flouquet, F. Honda, and D. Aoki, Multiple superconducting phases in a nearly ferromagnetic system, *Communications Physics* **2**, 147 (2019).
- [18] C. Girod, C. R. Stevens, A. Huxley, E. D. Bauer, F. B. Santos, J. D. Thompson, R. M. Fernandes, J.-X. Zhu, F. Ronning, P. F. S. Rosa, and S. M. Thomas, Thermodynamic and electrical transport properties of UTe₂ under uniaxial stress, *Physical Review B* **106**, L121101 (2022).
- [19] M. E. Barber, F. Lechermann, S. V. Streltsov, S. L. Skornyakov, S. Ghosh, B. Ramshaw, N. Kikugawa, D. A. Sokolov, A. P. Mackenzie, C. W. Hicks, *et al.*, Role of correlations in determining the Van Hove strain in Sr₂RuO₄, *Physical Review B* **100**, 245139 (2019).
- [20] Y.-S. Li, M. Garst, J. Schmalian, S. Ghosh, N. Kikugawa, D. A. Sokolov, C. W. Hicks, F. Jerzembeck, M. S. Ikeda, Z. Hu, B. J. Ramshaw, A. W. Rost, M. Nicklas, and A. P. Mackenzie, Elastocaloric determination of the phase diagram of Sr₂RuO₄, *Nature* **607**, 276 (2022).
- [21] M. D. Bachmann, G. M. Ferguson, F. Theuss, T. Meng, C. Putzke, T. Helm, K. R. Shirer, Y.-S. Li, K. A. Modic, M. Nicklas, M. König, D. Low, S. Ghosh, A. P. Mackenzie, F. Arnold, E. Hassinger, R. D. McDonald, L. E. Winter, E. D. Bauer, F. Ronning, B. J. Ramshaw, K. C. Nowack, and P. J. W. Moll, Spatial control of heavy-

- fermion superconductivity in CeIrIn₅, *Science* **366**, 221 (2019).
- [22] G. Liu and J. Maynard, Measuring elastic constants of arbitrarily shaped samples using resonant ultrasound spectroscopy, *The Journal of the Acoustical Society of America* **131**, 2068 (2012).
- [23] J. Plesek, R. Kolman, and M. Landa, Using finite element method for the determination of elastic moduli by resonant ultrasound spectroscopy, *The Journal of the Acoustical Society of America* **116**, 282 (2004).
- [24] B. J. Ramshaw, A. Shekhter, R. D. McDonald, J. B. Betts, J. N. Mitchell, P. H. Tobash, C. H. Mielke, E. D. Bauer, and A. Migliori, Avoided valence transition in a plutonium superconductor, *Proceedings of the National Academy of Sciences of the United States of America* **112**, 3285 (2015).
- [25] A. Shragai, F. Theuss, G. Grissonnanche, and B. J. Ramshaw, Rapid method for computing the mechanical resonances of irregular objects, *The Journal of the Acoustical Society of America* **153**, 119 (2023).
- [26] F. F. Balakirev, S. M. Ennaceur, R. J. Migliori, B. Maiorov, and A. Migliori, Resonant ultrasound spectroscopy: The essential toolbox, *Review of Scientific Instruments* **90**, 121401 (2019).
- [27] P. Ravindran, L. Fast, P. A. Korzhavyi, B. Johansson, J. Wills, and O. Eriksson, Density functional theory for calculation of elastic properties of orthorhombic crystals: Application to TiSi₂, *Journal of Applied Physics* **84**, 4891 (1998).
- [28] M. Weinert, G. Schneider, R. Podloucky, and J. Redinger, FLAPW: Applications and implementations, *J. Phys. Condens. Matter* **21**, 084201 (2009).
- [29] J. P. Perdew, K. Burke, and M. Ernzerhof, Generalized Gradient Approximation Made Simple, *Physical Review Letters* **77**, 3865 (1996).
- [30] S. Ikeda, H. Sakai, D. Aoki, Y. Homma, E. Yamamoto, A. Nakamura, Y. Shiokawa, Y. Haga, and Y. Ōnuki, Single Crystal Growth and Magnetic Properties of UTe₂, *Journal of the Physical Society of Japan* **75**, 116 (2006).
- [31] R. O. Bell and G. Rupprecht, Elastic Constants of Strontium Titanate, *Physical Review* **129**, 90 (1963).
- [32] E. Poindexter and A. A. Giardini, Elastic Constants of Strontium Titanate (SrTiO₃), *Physical Review* **110**, 1069 (1958).
- [33] F. Theuss, S. Ghosh, T. Chen, O. Tchernyshyov, S. Nakatsuji, and B. J. Ramshaw, Strong magnetoelastic coupling in Mn₃X (X = Ge, Sn), *Physical Review B* **105**, 174430 (2022).
- [34] R. Storn and K. Price, Differential Evolution – A Simple and Efficient Heuristic for global Optimization over Continuous Spaces, *Journal of Global Optimization* **11**, 341 (1997).
- [35] S. M. Thomas, F. B. Santos, M. H. Christensen, T. Asaba, F. Ronning, J. D. Thompson, E. D. Bauer, R. M. Fernandes, G. Fabbris, and P. F. S. Rosa, Evidence for a pressure-induced antiferromagnetic quantum critical point in intermediate-valence UTe₂, *Science Advances* **6**, eabc8709 (2020).
- [36] R. Storn and K. Price, Differential evolution—a simple and efficient heuristic for global optimization over continuous spaces, *Journal of global optimization* **11**, 341 (1997).
- [37] P. Virtanen, R. Gommers, T. E. Oliphant, M. Haberland, T. Reddy, D. Cournapeau, E. Burovski, P. Peterson, W. Weckesser, J. Bright, S. J. van der Walt, M. Brett, J. Wilson, K. J. Millman, N. Mayorov, A. R. J. Nelson, E. Jones, R. Kern, E. Larson, C. J. Carey, Í. Polat, Y. Feng, E. W. Moore, J. VanderPlas, D. Laxalde, J. Perktold, R. Cimrman, I. Henriksen, E. A. Quintero, C. R. Harris, A. M. Archibald, A. H. Ribeiro, F. Pedregosa, P. van Mulbregt, and SciPy 1.0 Contributors, SciPy 1.0: Fundamental Algorithms for Scientific Computing in Python, *Nature Methods* **17**, 261 (2020).

VII. SUPPLEMENTARY INFORMATION

VII.1. Bulk Modulus, Young's Moduli, and Poisson's Ratios

In [Table IV](#) we present the bulk modulus B , the Young's moduli E_{xx} , E_{yy} , E_{zz} , and the Poisson's ratios ν_{xz} , ν_{yz} , ν_{xy} for all measured samples and fits, calculated from the elastic moduli shown in the main text. For cubic SrTiO₃, $E_{xx} = E_{yy} = E_{zz}$ and $\nu_{xz} = \nu_{yz} = \nu_{xy}$, whereas for hexagonal Mn₃Ge, $E_{xx} = E_{yy}$ and $\nu_{xz} = \nu_{yz}$. For orthorhombic UTe₂, all moduli differ.

Sample	B (GPa)	Young's Moduli (GPa)			Poisson's Ratios		
		E_{xx}	E_{yy}	E_{zz}	ν_{xz}	ν_{yz}	ν_{xy}
SrTiO ₃	A	177	271	-	-	0.24	-
	B	174	266	-	-	0.25	-
Mn ₃ Ge	A	66	115	-	200	0.04	-
	B	65	114	-	201	0.05	-
UTe ₂	300 K	55	678	126	71	0.38	0.27
	4 K	57	71	131	74	0.40	0.26
						0.11	0.09

TABLE IV. Bulk modulus and Young's moduli

VII.2. Density Functional Theory

In [Table V](#) we compare the elastic moduli from density functional theory obtained from calculations during which the atomic coordinates were frozen to experimental values to calculations in which they were optimized. We also compare to calculations presented in the supplement of [\[18\]](#).

Method	c_{11}	c_{22}	c_{33}	c_{12}	c_{13}	c_{23}	c_{44}	c_{55}	c_{66}
coordinates frozen	100.2	140.0	99.3	28.7	56.4	27.1	33.8	69.4	36.1
coordinates optimized	95.7	136.0	89.7	28.1	46.0	26.0	28.0	57.1	31.0
Girod et al. [18]	97.0	140.7	101.3	40.9	48.6	46.7	19.6	57.3	27.1

TABLE V. UTe₂ DFT elastic tensor. Presented are the elastic moduli from density functional theory calculations. The first two rows are our calculations with atomic coordinates frozen to the experimental values and optimized. The last row are values given in the SI of [\[18\]](#), where the atomic coordinates were allowed to relax during minimization.

VII.3. Sample Digitization

Three-dimensional digitizations of the samples were obtained with a Zeiss Xradia Versa XRM-520 X-ray nano-CT. The average mesh size varies between samples and RUS solver methods (i.e. SMI vs. FEM). The meshes used for all FEM fits are shown in [Figure 2](#), and the average mesh size for all fits (FEM and SMI) are given in [Table VI](#). We used smaller meshes for irregularly-shaped samples (compared to regularly shaped ones) as well as for fits using the SMI method (compared to the FEM method). The latter is because a smaller mesh size increases the time for a fit to converge significantly for the FEM method, but leaves it almost unaffected for the SMI method [\[25\]](#).

Method	SrTiO ₃ sample A	SrTiO ₃ sample B	Mn ₃ Ge sample A	Mn ₃ Ge sample B	UTe ₂
FEM	84	56	52	40	-
SMI	60	5	23	5	9

TABLE VI. Mesh Size. Average distance between two vertices (in μm) in the meshes used in the RUS fits.

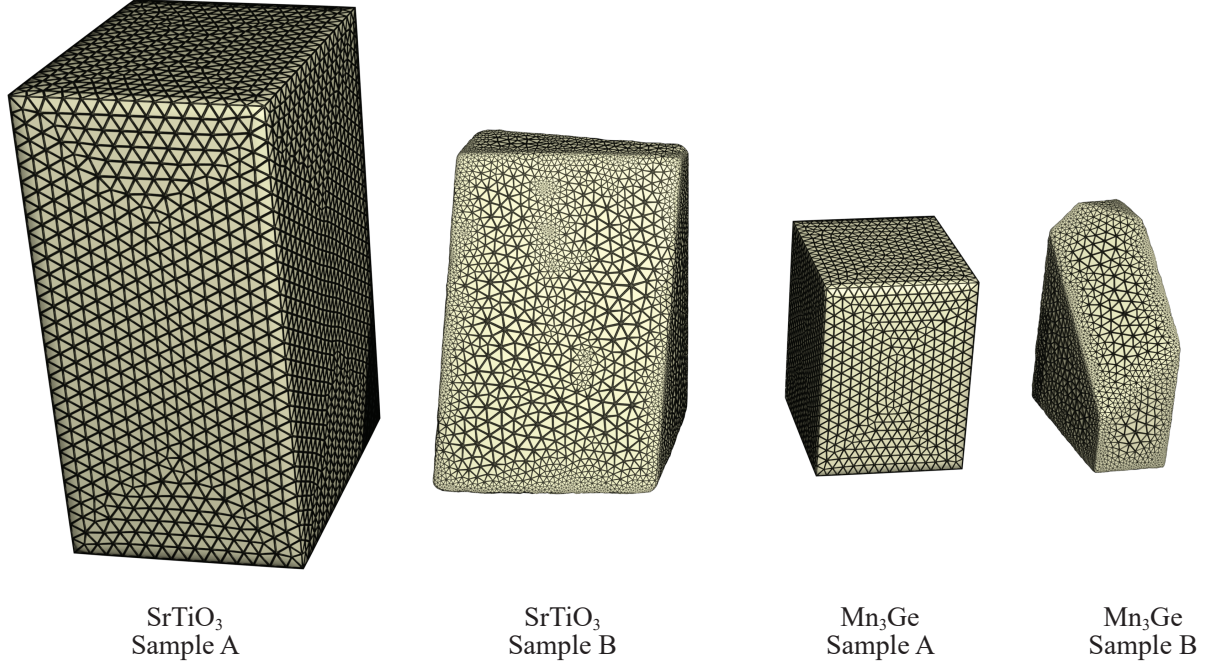


FIG. 2. **CT-Scan Meshes.** Shown are (from left to right) the digitizations for the SrTiO₃ (samples A, B) and Mn₃Ge (samples A, B) samples used for the RUS fits with the FEM method. Meshes for fits using the SMI method are too dense for individual faces to be identifiable on the shown scale.

VII.4. Differential Evolution Algorithm

We use a differential evolution global minimizer to extract the elastic moduli from the experimental resonance spectra [24, 36, 37]. A differential evolution algorithm is initialized with its first generation by randomly generating N sets of elastic moduli within given bounds. We call these sets parent sets, x_i^{parent} , $i \in [1, 2, \dots, N]$. Here every x_i^{parent} is a vector containing the independent elastic moduli of a given material. A resonance spectrum is then calculated for all parent sets (see discussion below on details on how resonances are calculated), and compared to the experimental resonance frequencies. The best set of elastic moduli x^{best} is characterized by the lowest χ^2 value. The second generation of the differential evolution algorithm is then created in three steps: First, a mutated set of elastic moduli x_i^{mut} is constructed for every parent set x_i^{parent} through

$$x_i^{mut} = x^{best} + \epsilon (x_j^{parent} + x_k^{parent}) . \quad (2)$$

Here, $j, k \in [1, N]$ are random indices, and the mutation parameter $\epsilon \in [0, 2]$ ensures a controlled perturbation of x^{best} . Secondly, trial sets x_i^{trial} are created from each mutated parameter set. For this procedure, each element $x_{i,j}^{trial}$ —i.e. each elastic modulus—of a given trial set is constructed as

$$x_{i,j}^{trial} = \begin{cases} x_{i,j}^{mut} & \text{if } rand(j) \leq p \text{ or } j = d \\ x_{i,j}^{parent} & \text{if } rand(j) > p \end{cases}, \quad (3)$$

where $rand(j) \in [0, 1]$ is a random number, $p \in [0, 1]$ is the crossover probability, and d is the number of elastic moduli. In the last step, each original parent set x_i^{parent} is compared to its related trial set x_i^{trial} and the set with smallest χ^2 value is chosen for the next generation. This procedure is repeated until the standard deviation of the residuals of a given generation falls below a predetermined tolerance level. The quality of this fit can be improved further by performing a gradient descent fit, using the results of the differential evolution algorithm as starting parameters.

VII.5. RUS Fit Uncertainties

The main sources of uncertainties in our fits are due to small deviations from the weak-coupling approximation used in our analysis and from small uncertainties in the alignment between the crystal axes and the sample mesh.

The former is caused by the weight of the cantilever holding the top ultrasonic transducer and causes the measured resonance frequencies to weakly depend on how the sample is mounted in the RUS apparatus. To estimate the resulting uncertainty in elastic moduli, we arranged all irregularly-shaped samples in three different ways between the transducers and re-performed RUS measurements and fits. Figure 3 illustrates the different arrangements of samples in the setup and the rows in Table VII show the respective elastic moduli (note that arrangement 2 is how the samples were mounted for the results shown in the main paper). This analysis leads to an average uncertainty of 1.7 GPa, 2.3 GPa, 0.5 GPa for SrTiO₃ sample B, Mn₃Ge sample B, and the UTe₂ sample at 300 K, respectively. The uncertainties are about a factor of 4 larger for the SrTiO₃ and Mn₃Ge samples since they were measured in a RUS apparatus with a cantilever weighing about 5 g, while the UTe₂ spectra were recorded in an apparatus with a cantilever weighing about 0.5 g.

The latter contribution originates in an uncertainty of about 1 degree to which we can align the crystal axes and the sample mesh using Laue backreflection diffractometry. Refitting our RUS resonance spectra with a sample mesh rotated by 1 degree results in average uncertainties of 0.4 GPa, 2 GPa, 0.5 GPa, for the elastic moduli of SrTiO₃ sample B, Mn₃Ge sample B, and UTe₂ at 300 K, respectively. Individual error bars for each elastic modulus due to sample misalignment are given in Table VII.

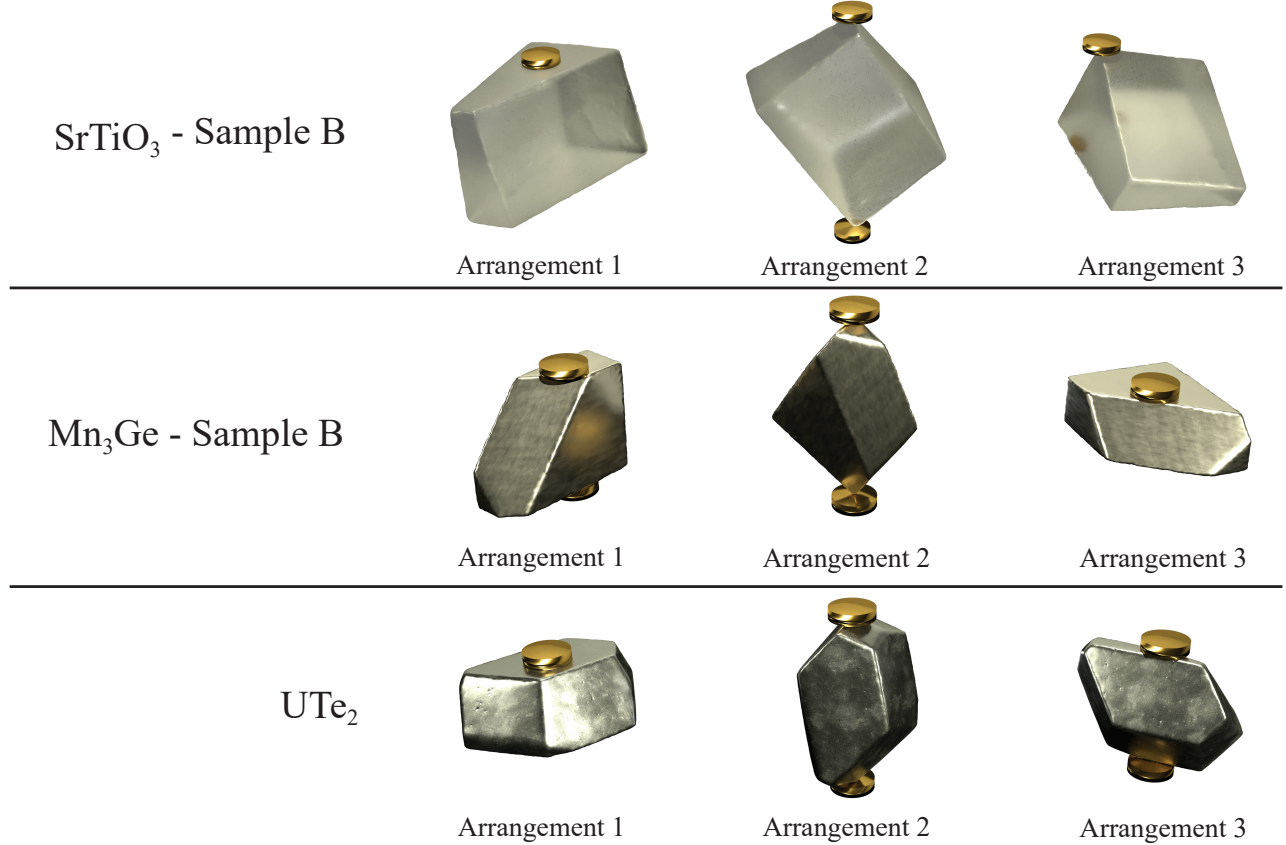


FIG. 3. RUS Sample Arrangements. Shown are different arrangements of the samples in the RUS apparatus. The golden discs represent the ultrasonic transducers (the bottom transducer is occluded by the sample in some images). The arrangement number relates to the correct row in Table VII.

VII.6. RUS Resonance Spectra and Fit Results

We show lists of experimental resonance frequencies f_{exp} along with the calculated frequencies f_{calc} corresponding to the RUS fit results in the main text. The lowest three resonances are excluded from all fits.

Sample	Arrangement	c_{11}	c_{22}	c_{33}	c_{12}	c_{13}	c_{23}	c_{44}	c_{55}	c_{66}
SrTiO ₃ (B)	1	313.8	-	-	100.3	-	-	122.62	-	-
	2	316.7±0.5	-	-	102.9±0.7	-	-	121.95±0.05	-	-
	3	315.8	-	-	100.2	-	-	122.30	-	-
Mn ₃ Ge (B)	1	126	-	200	38	12	-	48.7	-	-
	2	127±1	-	203±2	40±2	14±5	-	48.7±0.5	-	-
	3	129	-	196	42	18	-	49.6	-	-
UTe ₂ (300 K)	1	84.4	139.0	92.0	25.6	38.1	32.0	26.9	52.3	29.4
	2	84.7±0.44	139.5±0.8	91.1±1.1	26.8±1.0	38.1±0.5	31.6±0.4	26.9±0.2	52.4±0.2	29.7±0.2
	3	83.8	140.3	90.6	25.5	37.2	31.6	27.1	52.3	29.4

TABLE VII. **RUS Uncertainty Analysis.** Fit results for the different arrangements of all irregularly-shaped samples shown in Figure 3 to estimate the uncertainty introduced by the weight of the cantilever holding the top ultrasonic transducer. For each sample and arrangement 2, we also show the errors caused by a 1 degree misalignment between the crystal axes and the sample mesh. All fits were performed with the SMI method.

TABLE VIII: SrTiO₃ sample A (regular shape)

Index	f_{exp} (MHz)	RPR		SMI		FEM	
		f_{calc} (MHz)	diff (%)	f_{calc} (MHz)	diff (%)	f_{calc} (MHz)	diff (%)
1	0.71037	0.70491	-	0.70491	-	0.70489	-
2	0.79197	0.79156	-	0.79156	-	0.79155	-
3	0.89772	0.90185	-	0.90185	-	0.90184	-
4	1.17353	1.17781	0.363	1.17781	0.363	1.17779	0.361
5	1.24570	1.24714	0.116	1.24714	0.116	1.24711	0.113
6	1.33132	1.32506	0.473	1.32506	0.473	1.32504	0.474
7	1.37709	1.38138	0.310	1.38138	0.310	1.38135	0.308
8	1.41735	1.40410	0.944	1.40410	0.944	1.40408	0.945
9	1.50363	1.49941	0.281	1.49941	0.281	1.49939	0.283
10	1.55724	1.55327	0.256	1.55327	0.256	1.55325	0.257
11	1.59727	1.58515	0.765	1.58515	0.765	1.58513	0.766
12	1.60045	1.58865	0.743	1.58865	0.743	1.58863	0.744
13	1.71219	1.71178	0.024	1.71178	0.024	1.71175	0.025
14	1.77642	1.77451	0.108	1.77451	0.108	1.77449	0.109
15	1.78574	1.79251	0.377	1.79251	0.377	1.79247	0.375
16	1.83710	1.84222	0.278	1.84222	0.277	1.84219	0.276
17	1.85498	1.85528	0.016	1.85528	0.016	1.85524	0.014
18	1.91594	1.92356	0.396	1.92356	0.396	1.92353	0.395
19	1.97811	1.97315	0.251	1.97315	0.251	1.97314	0.252
20	1.98353	1.98541	0.095	1.98541	0.095	1.98538	0.093
21	2.03547	2.04563	0.496	2.04563	0.496	2.04559	0.495
22	2.07281	2.07985	0.338	2.07985	0.338	2.07982	0.337
23	2.16306	2.17696	0.638	2.17696	0.639	2.17695	0.638
24	2.17570	2.17867	0.136	2.17867	0.136	2.17864	0.135
25	2.20327	2.21156	0.375	2.21156	0.375	2.21154	0.374
26	2.20830	2.21607	0.350	2.21607	0.350	2.21606	0.350
27	2.22903	2.22728	0.078	2.22728	0.078	2.22727	0.079
28	2.23226	2.23763	0.240	2.23763	0.240	2.23761	0.239
29	2.23351	2.23846	0.221	2.23846	0.221	2.23845	0.221
30	2.28139	2.27258	0.388	2.27258	0.388	2.27258	0.388
31	2.32126	2.31051	0.465	2.31051	0.465	2.31052	0.465
32	2.33100	2.32182	0.395	2.32182	0.395	2.32180	0.396
33	2.34719	2.34083	0.272	2.34083	0.272	2.34082	0.272
34	2.44146	2.44675	0.216	2.44675	0.216	2.44674	0.216
35	2.46013	2.45143	0.355	2.45142	0.355	2.45144	0.355
36	2.50210	2.50958	0.298	2.50958	0.298	2.50956	0.297
37	2.50662	2.50968	0.122	2.50968	0.122	2.50965	0.121
38	2.53756	2.53887	0.051	2.53887	0.051	2.53889	0.052
39	2.57650	2.57679	0.011	2.57679	0.011	2.57680	0.012
40	2.58500	2.59496	0.384	2.59496	0.384	2.59496	0.384
41	2.59850	2.59922	0.028	2.59922	0.028	2.59920	0.027
42	2.62865	2.63115	0.095	2.63116	0.095	2.63117	0.096
43	2.65167	2.65229	0.023	2.65229	0.023	2.65226	0.022

Table 2 continued on next page.

Table 2 continued.

Index	f_{exp} (MHz)	RPR		SMI		FEM	
		f_{calc} (MHz)	diff (%)	f_{calc} (MHz)	diff (%)	f_{calc} (MHz)	diff (%)
44	2.68309	2.68338	0.011	2.68338	0.011	2.68338	0.011
45	2.70518	2.70901	0.141	2.70901	0.141	2.70898	0.140
46	2.74782	2.74881	0.036	2.74881	0.036	2.74883	0.037
47	2.75176	2.75107	0.025	2.75107	0.025	2.75107	0.025
48	2.75392	2.76091	0.253	2.76091	0.253	2.76092	0.254
49	2.78789	2.79403	0.220	2.79403	0.220	2.79408	0.221
50	2.80071	2.79544	0.189	2.79545	0.188	2.79545	0.188
51	2.82197	2.82346	0.053	2.82346	0.053	2.82352	0.055
52	2.84439	2.85166	0.255	2.85167	0.255	2.85166	0.255
53	2.91635	2.91928	0.101	2.91928	0.101	2.91931	0.102
54	2.92322	2.92473	0.051	2.92473	0.051	2.92478	0.053
55	2.94885	2.92904	0.677	2.92904	0.677	2.92902	0.677
56	3.00333	2.99929	0.135	2.99929	0.135	2.99940	0.131
57	3.01642	3.01070	0.190	3.01070	0.190	3.01074	0.189
58	3.03353	3.03246	0.035	3.03246	0.036	3.03254	0.033
59	3.03869	3.04328	0.151	3.04328	0.151	3.04332	0.152
60	3.06889	3.06572	0.103	3.06572	0.103	3.06574	0.103
61	3.13815	3.14283	0.149	3.14283	0.149	3.14288	0.151
62	3.15099	3.15332	0.074	3.15332	0.074	3.15339	0.076
63	3.15918	3.16111	0.061	3.16111	0.061	3.16112	0.062
64	3.16664	3.16975	0.098	3.16975	0.098	3.16985	0.101
65	3.22486	3.22895	0.127	3.22895	0.127	3.22893	0.126
66	3.22600	3.23110	0.158	3.23110	0.158	3.23107	0.157
67	3.25102	3.24020	0.334	3.24020	0.334	3.24033	0.330
68	3.25333	3.24905	0.132	3.24905	0.132	3.24915	0.129
69	3.26656	3.25129	0.470	3.25129	0.470	3.25141	0.466
70	3.27348	3.28127	0.237	3.28127	0.237	3.28131	0.239

TABLE IX: SrTiO₃ sample B (irregular shape)

Index	f_{exp} (MHz)	SMI		FEM	
		f_{calc} (MHz)	diff (%)	f_{calc} (MHz)	diff (%)
1	1.10869	1.09168	-	1.09156	-
2	1.20480	1.19121	-	1.19112	-
3	1.52331	1.50347	-	1.50341	-
4	1.88059	1.86636	0.762	1.86620	0.771
5	1.97243	1.97144	0.050	1.97135	0.055
6	1.98450	1.98777	0.164	1.98756	0.154
7	2.07997	2.07118	0.424	2.07100	0.433
8	2.15054	2.14467	0.274	2.14453	0.280
9	2.23955	2.23207	0.335	2.23186	0.344
10	2.37823	2.36840	0.415	2.36833	0.418
11	2.43553	2.44027	0.194	2.44001	0.184
12	2.58487	2.57275	0.471	2.57258	0.478
13	2.72511	2.71927	0.215	2.71912	0.220
14	2.80098	2.79093	0.360	2.79078	0.366
15	2.83415	2.83210	0.072	2.83199	0.077
16	2.87280	2.86311	0.339	2.86304	0.341
17	2.92701	2.91494	0.414	2.91473	0.421
18	3.07796	3.07446	0.114	3.07432	0.118
19	3.13235	3.14863	0.517	3.14864	0.517
20	3.16734	3.16494	0.076	3.16486	0.079
21	3.18282	3.18195	0.027	3.18191	0.029
22	3.25382	3.24307	0.331	3.24298	0.334
23	3.29615	3.29027	0.179	3.29022	0.180
24	3.31731	3.33535	0.541	3.33524	0.538
25	3.48056	3.50474	0.690	3.50469	0.688
26	3.51006	3.52415	0.400	3.52412	0.399
27	3.65645	3.66182	0.147	3.66178	0.145
28	3.78318	3.79193	0.231	3.79191	0.230
29	3.84523	3.84207	0.082	3.84198	0.085

Table 3 continued on next page.

Table 3 continued.

Index	f_{exp} (MHz)	SMI		FEM	
		f_{calc} (MHz)	diff (%)	f_{calc} (MHz)	diff (%)
30	3.89894	3.90375	0.123	3.90368	0.122
31	3.98772	3.99729	0.239	3.99727	0.239
32	4.00064	4.00409	0.086	4.00407	0.086
33	4.06006	4.04985	0.252	4.04979	0.254
34	4.10005	4.10447	0.108	4.10444	0.107
35	4.15255	4.14028	0.296	4.14022	0.298
36	4.18979	4.20182	0.286	4.20174	0.284
37	4.23696	4.22814	0.209	4.22819	0.207
38	4.27449	4.28863	0.330	4.28857	0.328
39	4.30861	4.31115	0.059	4.31124	0.061
40	4.34986	4.35327	0.078	4.35335	0.080
41	4.39819	4.39097	0.165	4.39113	0.161
42	4.46403	4.46713	0.069	4.46719	0.071
43	4.48597	4.47481	0.249	4.47493	0.247
44	4.63845	4.62951	0.193	4.62957	0.192
45	4.68243	4.69013	0.164	4.69022	0.166
46	4.74359	4.74395	0.008	4.74417	0.012
47	4.75697	4.76987	0.270	4.76996	0.272
48	4.80223	4.79540	0.142	4.79552	0.140
49	4.82394	4.84266	0.387	4.84274	0.388
50	4.89389	4.90448	0.216	4.90445	0.215
51	4.93746	4.93653	0.019	4.93677	0.014
52	4.98372	4.98686	0.063	4.98700	0.066
53	5.00140	5.00252	0.022	5.00247	0.021
54	5.03260	5.03444	0.037	5.03457	0.039
55	5.06065	5.06660	0.117	5.06673	0.120
56	5.10892	5.10434	0.090	5.10460	0.085
57	5.12704	5.12970	0.052	5.12991	0.056
58	5.16940	5.18029	0.210	5.18061	0.216
59	5.20187	5.23093	0.556	5.23130	0.562
60	5.25259	5.25272	0.002	5.25278	0.004
61	5.27776	5.27884	0.020	5.27913	0.026
62	5.28863	5.29927	0.201	5.29969	0.209
63	5.33266	5.33158	0.020	5.33170	0.018
64	5.37012	5.35725	0.240	5.35743	0.237
65	5.40014	5.39589	0.079	5.39627	0.072
66	5.43224	5.43571	0.064	5.43599	0.069
67	5.45845	5.45699	0.027	5.45728	0.021
68	5.49232	5.49778	0.099	5.49816	0.106
69	5.54920	5.55358	0.079	5.55405	0.087
70	5.58061	5.58871	0.145	5.58914	0.153

TABLE X: Mn₃Ge sample A (regular shape)

Index	f_{exp} (MHz)	RPR		SMI		FEM	
		f_{calc} (MHz)	diff (%)	f_{calc} (MHz)	diff (%)	f_{calc} (MHz)	diff (%)
1	0.96469	0.95542	-	0.95544	-	0.95531	-
2	1.31011	1.31762	-	1.31764	-	1.31751	-
3	1.46748	1.46874	-	1.46876	-	1.46855	-
4	1.50955	1.50952	0.002	1.50951	0.002	1.50947	0.005
5	1.56402	1.56137	0.169	1.56136	0.170	1.56127	0.176
6	1.57830	1.57952	0.077	1.57951	0.077	1.57945	0.073
7	1.58425	1.60049	1.015	1.60051	1.016	1.60029	1.002
8	1.60141	1.61340	0.743	1.61340	0.743	1.61327	0.735
9	1.60582	1.61949	0.845	1.61951	0.846	1.61938	0.838
10	1.78631	1.80175	0.857	1.80177	0.858	1.80162	0.850
11	1.82036	1.81183	0.471	1.81182	0.471	1.81169	0.478
12	1.87303	1.87322	0.010	1.87322	0.010	1.87313	0.005
13	1.94132	1.93235	0.464	1.93233	0.465	1.93222	0.471
14	1.95112	1.95456	0.176	1.95455	0.175	1.95451	0.173
15	2.03329	2.02996	0.164	2.02997	0.164	2.02986	0.169

Table 4 continued on next page.

Table 4 continued.

Index	f_{exp} (MHz)	RPR		SMI		FEM	
		f_{calc} (MHz)	diff (%)	f_{calc} (MHz)	diff (%)	f_{calc} (MHz)	diff (%)
16	2.09609	2.08355	0.602	2.08353	0.603	2.08339	0.610
17	2.10555	2.10872	0.150	2.10867	0.148	2.10854	0.142
18	2.14587	2.12376	1.041	2.12373	1.043	2.12363	1.047
19	2.16239	2.17045	0.371	2.17041	0.369	2.17050	0.374
20	2.16541	2.17570	0.473	2.17572	0.474	2.17548	0.463
21	2.25310	2.26434	0.496	2.26437	0.497	2.26423	0.491
22	2.32002	2.30809	0.517	2.30807	0.518	2.30797	0.522
23	2.37049	2.35061	0.846	2.35060	0.846	2.35052	0.849
24	2.38275	2.38340	0.027	2.38330	0.023	2.38334	0.024
25	2.43586	2.41898	0.698	2.41896	0.699	2.41890	0.701
26	2.46256	2.47420	0.471	2.47422	0.471	2.47413	0.468
27	2.47301	2.47498	0.080	2.47498	0.080	2.47483	0.073
28	2.52384	2.55083	1.058	2.55069	1.053	2.55063	1.051
29	2.55464	2.57203	0.676	2.57205	0.677	2.57190	0.671
30	2.57758	2.59117	0.524	2.59118	0.525	2.59105	0.520
31	2.61331	2.62284	0.363	2.62282	0.363	2.62273	0.359
32	2.65457	2.64939	0.196	2.64940	0.195	2.64940	0.195
33	2.71919	2.72259	0.125	2.72258	0.124	2.72248	0.121
34	2.75160	2.74615	0.198	2.74616	0.198	2.74602	0.203
35	2.78098	2.77733	0.131	2.77734	0.131	2.77722	0.135
36	2.84224	2.83905	0.112	2.83904	0.113	2.83904	0.113
37	2.86041	2.86306	0.092	2.86298	0.090	2.86289	0.086
38	2.87166	2.86844	0.112	2.86847	0.111	2.86843	0.113
39	2.91103	2.92610	0.515	2.92611	0.516	2.92617	0.518
40	2.93140	2.92769	0.127	2.92770	0.126	2.92756	0.131
41	2.93455	2.93191	0.090	2.93190	0.090	2.93189	0.091
42	2.94156	2.94237	0.027	2.94237	0.028	2.94228	0.024
43	3.04438	3.05124	0.225	3.05123	0.224	3.05109	0.220
44	3.10644	3.09616	0.332	3.09616	0.332	3.09622	0.330
45	3.12912	3.13303	0.125	3.13303	0.125	3.13297	0.123
46	3.19343	3.17795	0.487	3.17796	0.487	3.17801	0.485
47	3.21141	3.21040	0.031	3.21041	0.031	3.21032	0.034
48	3.28658	3.28210	0.136	3.28212	0.136	3.28219	0.134
49	3.30955	3.29828	0.342	3.29828	0.342	3.29851	0.335
50	3.31565	3.32261	0.209	3.32261	0.209	3.32258	0.209
51	3.35754	3.37386	0.484	3.37387	0.484	3.37382	0.482
52	3.38287	3.37789	0.147	3.37786	0.148	3.37795	0.146
53	3.44121	3.45795	0.484	3.45795	0.484	3.45796	0.484
54	3.47190	3.46067	0.324	3.46069	0.324	3.46107	0.313
55	3.49421	3.48695	0.208	3.48694	0.208	3.48696	0.208
56	3.49812	3.50059	0.071	3.50057	0.070	3.50061	0.071
57	3.49964	3.51232	0.361	3.51236	0.362	3.51229	0.360
58	3.54746	3.53238	0.427	3.53237	0.427	3.53259	0.421
59	3.57278	3.56487	0.222	3.56488	0.222	3.56526	0.211
60	3.58496	3.57191	0.365	3.57191	0.365	3.57200	0.363
61	3.58767	3.59720	0.265	3.59714	0.263	3.59709	0.262
62	3.60231	3.60308	0.022	3.60311	0.022	3.60304	0.020
63	3.60760	3.60521	0.066	3.60521	0.066	3.60540	0.061
64	3.61308	3.60655	0.181	3.60655	0.181	3.60663	0.179
65	3.61436	3.61431	0.001	3.61432	0.001	3.61455	0.005
66	3.61865	3.62068	0.056	3.62069	0.057	3.62084	0.060
67	3.64765	3.64158	0.167	3.64152	0.168	3.64153	0.168
68	3.67018	3.64580	0.669	3.64580	0.669	3.64602	0.663
69	3.71718	3.70179	0.416	3.70179	0.416	3.70203	0.409
70	3.72327	3.72386	0.016	3.72386	0.016	3.72412	0.023
71	3.78761	3.79633	0.230	3.79635	0.230	3.79659	0.237
72	3.81140	3.80554	0.154	3.80556	0.153	3.80579	0.147
73	3.84430	3.82293	0.559	3.82295	0.559	3.82310	0.554
74	3.86988	3.84886	0.546	3.84885	0.546	3.84915	0.539
75	3.91723	3.91340	0.098	3.91339	0.098	3.91352	0.095
76	3.94563	3.92345	0.565	3.92345	0.565	3.92395	0.552

Table 4 continued on next page.

Table 4 continued.

Index	f_{exp} (MHz)	RPR		SMI		FEM	
		f_{calc} (MHz)	diff (%)	f_{calc} (MHz)	diff (%)	f_{calc} (MHz)	diff (%)
77	3.97908	3.97784	0.031	3.97787	0.030	3.97802	0.027
78	3.99942	3.99986	0.011	3.99985	0.011	4.00031	0.022
79	4.01915	4.00900	0.253	4.00903	0.252	4.00943	0.242
80	4.03495	4.02355	0.284	4.02355	0.283	4.02443	0.262
81	4.04595	4.06045	0.357	4.06046	0.357	4.06074	0.364
82	4.05758	4.06567	0.199	4.06558	0.197	4.06568	0.199
83	4.06491	4.08637	0.525	4.08631	0.524	4.08631	0.524
84	4.0780	4.09008	0.295	4.09004	0.294	4.09015	0.297

TABLE XI: Mn₃Ge sample B (irregular shape)

Index	f_{exp} (MHz)	SMI		FEM	
		f_{calc} (MHz)	diff (%)	f_{calc} (MHz)	diff (%)
1	0.77100	0.72927	-	0.72932	-
2	1.08478	1.06421	-	1.06356	-
3	1.22382	1.21029	-	1.21031	-
4	1.33437	1.32618	0.618	1.32623	0.614
5	1.44953	1.43028	1.346	1.43030	1.344
6	1.60718	1.59563	0.723	1.59565	0.722
7	1.86078	1.84572	0.816	1.84544	0.831
8	1.88524	1.88848	0.172	1.88804	0.148
9	2.02059	2.01970	0.044	2.01929	0.064
10	2.06617	2.03724	1.420	2.03660	1.452
11	2.12700	2.11597	0.521	2.11593	0.523
12	2.30712	2.29890	0.358	2.29885	0.360
13	2.33951	2.33223	0.312	2.33215	0.316
14	2.44134	2.43977	0.064	2.43948	0.076
15	2.48376	2.48460	0.034	2.48477	0.040
16	2.66501	2.66902	0.150	2.66862	0.135
17	2.75780	2.74510	0.463	2.74453	0.484
18	2.78254	2.78677	0.152	2.78699	0.160
19	2.83647	2.82217	0.507	2.82196	0.514
20	2.97943	2.99342	0.467	2.99356	0.472
21	3.01159	3.01770	0.203	3.01823	0.220
22	3.07402	3.09174	0.573	3.09132	0.560
23	3.13148	3.13824	0.215	3.13768	0.198
24	3.16311	3.17632	0.416	3.17606	0.408
25	3.24362	3.25436	0.330	3.25461	0.338
26	3.25447	3.27058	0.492	3.27034	0.485
27	3.30929	3.30305	0.189	3.30309	0.188
28	3.40908	3.42759	0.540	3.42754	0.539
29	3.46136	3.46796	0.190	3.46799	0.191
30	3.53828	3.52248	0.449	3.52213	0.459
31	3.58063	3.59778	0.477	3.59745	0.468
32	3.64885	3.64490	0.108	3.64495	0.107
33	3.70451	3.68606	0.500	3.68572	0.510
34	3.73124	3.74476	0.361	3.74458	0.356
35	3.77514	3.78817	0.344	3.78828	0.347
36	3.81664	3.81972	0.081	3.82010	0.091
37	3.84659	3.86236	0.408	3.86303	0.426
38	3.89301	3.90315	0.260	3.90408	0.283
39	3.92147	3.92013	0.034	3.92011	0.035
40	4.00155	4.01985	0.455	4.01957	0.448
41	4.05232	4.04810	0.104	4.04792	0.109
42	4.07279	4.07673	0.096	4.07692	0.101
43	4.11185	4.10555	0.154	4.10515	0.163
44	4.16568	4.12779	0.918	4.12750	0.925
45	4.17169	4.15185	0.478	4.15181	0.479
46	4.23171	4.23428	0.061	4.23422	0.059
47	4.25632	4.26175	0.127	4.26195	0.132
48	4.28696	4.29318	0.145	4.29333	0.148

Table 5 continued on next page.

Table 5 continued.

Index	f_{exp} (MHz)	SMI		FEM	
		f_{calc} (MHz)	diff (%)	f_{calc} (MHz)	diff (%)
49	4.33501	4.33233	0.062	4.33252	0.057
50	4.39232	4.39776	0.124	4.39806	0.131
51	4.44617	4.44492	0.028	4.44480	0.031
52	4.45932	4.45990	0.013	4.45953	0.005
53	4.47269	4.48323	0.235	4.48383	0.248
54	4.50973	4.51226	0.056	4.51274	0.067
55	4.54993	4.53911	0.239	4.53896	0.242
56	4.57564	4.59124	0.340	4.59160	0.348
57	4.61763	4.59924	0.400	4.59942	0.396
58	4.64177	4.63850	0.070	4.63892	0.061
59	4.67340	4.67170	0.036	4.67168	0.037
60	4.67725	4.71140	0.725	4.71268	0.752
61	4.74328	4.72813	0.320	4.72823	0.318
62	4.75405	4.76937	0.321	4.76985	0.331
63	4.78548	4.79885	0.279	4.79964	0.295
64	4.83816	4.84783	0.199	4.84855	0.214
65	4.87454	4.89056	0.328	4.89094	0.335
66	4.89770	4.89955	0.038	4.89976	0.042
67	4.91976	4.92224	0.050	4.92262	0.058
68	4.94198	4.93395	0.163	4.93404	0.161
69	4.97544	4.95930	0.326	4.95855	0.341
70	5.00234	4.98595	0.329	4.98635	0.321
71	5.05521	5.05121	0.079	5.05153	0.073
72	5.06222	5.07826	0.316	5.07871	0.325
73	5.10734	5.10605	0.025	5.10572	0.032
74	5.14001	5.15663	0.322	5.15649	0.320
75	5.17375	5.18850	0.284	5.18928	0.299
76	5.20031	5.19720	0.060	5.19750	0.054
77	5.22839	5.23149	0.059	5.23154	0.060
78	5.24876	5.27701	0.535	5.27763	0.547
79	5.31483	5.33671	0.410	5.33550	0.387
80	5.35238	5.35144	0.018	5.35154	0.016
81	5.36938	5.36972	0.006	5.36912	0.005
82	5.37790	5.40947	0.584	5.40967	0.587
83	5.41390	5.42943	0.286	5.42989	0.295
84	5.43467	5.44317	0.156	5.44304	0.154

TABLE XII: UTe₂ SMI fit results

Index	300 K			4 K		
	f_{exp} (MHz)	f_{calc} (MHz)	diff (%)	f_{exp} (MHz)	f_{calc} (MHz)	diff (%)
1	0.64645	0.64254	-	0.66344	0.65765	-
2	0.80333	0.80092	-	0.81724	0.81425	-
3	0.86443	0.85869	-	0.87702	0.87984	-
4	1.09564	1.09407	0.143	1.11952	1.12080	0.114
5	1.18679	1.18992	0.263	1.21970	1.21818	0.125
6	1.32441	1.32471	0.023	1.34208	1.34680	0.350
7	1.34023	1.33357	0.499	1.36327	1.35737	0.435
8	1.49544	1.49019	0.353	1.51789	1.51792	0.002
9	1.56441	1.57149	0.450	1.59618	1.60073	0.284
10	1.64031	1.64096	0.040	1.67269	1.67216	0.032
11	1.67848	1.67996	0.088	1.71445	1.71359	0.050
12	1.71675	1.71182	0.288	1.75060	1.74551	0.291
13	1.77448	1.77473	0.014	1.80806	1.80856	0.028
14	1.83771	1.83767	0.002	1.87151	1.87196	0.024
15	1.86861	1.86685	0.094	1.90573	1.90183	0.205
16	1.93964	1.93352	0.317	1.97323	1.97067	0.130
17	2.02902	2.02240	0.327	2.06927	2.06282	0.313
18	2.06086	2.06388	0.146	2.09666	2.10371	0.335
19	2.13401	2.13646	0.115	2.17374	2.17693	0.147
20	2.18310	2.17778	0.244	2.23096	2.22600	0.223

Table 6 continued on next page.

Table 6 continued.

Index	300 K			4 K		
	f_{exp} (MHz)	f_{calc} (MHz)	diff (%)	f_{exp} (MHz)	f_{calc} (MHz)	diff (%)
21	2.21720	2.21601	0.054	2.26583	2.25830	0.334
22	2.25887	2.25321	0.251	2.30249	2.29602	0.282
23	2.27636	2.28024	0.170	2.32310	2.32435	0.054
24	2.33423	2.33367	0.024	2.37609	2.37215	0.166
25	2.35896	2.35370	0.223	2.40235	2.40166	0.029
26	2.37195	2.37131	0.027	2.41002	2.41040	0.016
27	2.40361	2.39962	0.166	2.46079	2.45405	0.275
28	2.45741	2.45189	0.225	2.50592	2.50395	0.079
29	2.47653	2.47529	0.050	2.51386	2.52139	0.299
30	2.49726	2.49516	0.085	2.55527	2.55033	0.194
31	2.53119	2.53407	0.113	2.58793	2.58510	0.109
32	2.56841	2.57293	0.176	2.61987	2.62518	0.202
33	2.58945	2.58640	0.118	2.64506	2.64006	0.189
34	2.67652	2.67401	0.094	2.72662	2.72716	0.020
35	2.69934	2.70106	0.064	2.75414	2.75458	0.016
36	2.70867	2.71641	0.285	2.76160	2.76697	0.194
37	2.75772	2.76163	0.142	2.81381	2.81674	0.104
38	2.80315	2.80522	0.073	2.85929	2.86408	0.167
39	2.83790	2.83401	0.137	2.88995	2.88518	0.165
40	2.84413	2.84397	0.006	2.89806	2.89733	0.025
41	2.85740	2.85678	0.022	2.91031	2.91158	0.044
42	2.89809	2.90021	0.073	2.95404	2.95353	0.017
43	2.91204	2.90687	0.178	2.96297	2.95926	0.125
44	2.93294	2.93629	0.114	2.98892	2.98868	0.008
45	2.97064	2.96887	0.060	3.03454	3.03881	0.140
46	2.98750	2.98376	0.125	3.04986	3.04773	0.070
47	3.04099	3.04359	0.086	3.10384	3.10431	0.015
48	3.05451	3.05513	0.020	3.11878	3.11603	0.088
49	3.07129	3.06617	0.167	3.12869	3.12381	0.156
50	3.11543	3.11631	0.028	3.17516	3.18070	0.174
51	3.14348	3.14681	0.106	3.21205	3.20841	0.113
52	3.16609	3.16333	0.087	3.23373	3.23001	0.115
53	3.19312	3.19392	0.025	3.25821	3.25521	0.092
54	3.21950	3.22107	0.049	3.28885	3.29187	0.092
55	3.26064	3.26213	0.046	3.32549	3.32873	0.097
56	3.27367	3.27710	0.105	3.33381	3.33748	0.110
57	3.28431	3.28793	0.110	3.35277	3.35414	0.041
58	3.33902	3.33560	0.103	3.39969	3.39764	0.060
59	3.37665	3.38210	0.161	3.44137	3.44067	0.020
60	3.38263	3.38841	0.171	3.44466	3.45563	0.317
61	3.40724	3.40264	0.135	3.47399	3.46879	0.150
62	3.42588	3.41984	0.176	3.48688	3.48075	0.176
63	3.46878	3.46450	0.123	3.52655	3.52462	0.055
64	3.48772	3.48306	0.134	3.55491	3.55194	0.084
65	3.49884	3.50575	0.197	3.56459	3.57159	0.196
66	3.51096	3.51080	0.005	3.58054	3.57953	0.028
67	3.54860	3.55098	0.067	3.61868	3.62048	0.050
68	3.56768	3.57417	0.182	3.64321	3.64728	0.112
69	3.57963	3.58351	0.108	3.65177	3.65702	0.144
70	3.59151	3.59154	0.001	3.66315	3.66157	0.043
71	3.63037	3.63146	0.030	3.70535	3.70318	0.059
72	3.66135	3.66185	0.014	3.73498	3.73249	0.067
73	3.67686	3.67367	0.087	3.75129	3.74617	0.137
74	3.70093	3.69729	0.098	3.77215	3.77270	0.015
75	3.72551	3.71979	0.154	3.79478	3.78954	0.138
76	3.74072	3.74038	0.009	3.81853	3.81297	0.146
77	3.75135	3.75430	0.079	3.82596	3.82515	0.021
78	3.76556	3.76595	0.010	3.83940	3.83786	0.040
79	3.77374	3.77640	0.071	3.84028	3.84954	0.240
80	3.81529	3.81717	0.049	3.89424	3.89363	0.016
81	3.84139	3.83861	0.072	3.91424	3.91245	0.046

Table 6 continued on next page.

Table 6 continued.

Index	300 K			4 K		
	f_{exp} (MHz)	f_{calc} (MHz)	diff (%)	f_{exp} (MHz)	f_{calc} (MHz)	diff (%)
82	3.85843	3.85711	0.034	3.93674	3.93303	0.094
83	3.87490	3.88271	0.201	3.94923	3.95735	0.205
84	3.89786	3.89296	0.126	3.97082	3.96312	0.194
85	3.90314	3.90305	0.002	3.98043	3.98563	0.130
86	3.91220	3.92250	0.263	3.98665	3.99710	0.261
87	3.94153	3.93803	0.089	4.01442	4.01238	0.051
88	3.99297	3.98031	0.318	4.06185	4.05116	0.264
89	3.99436	3.99491	0.014	4.07113	4.06908	0.050
90	4.00126	4.01160	0.258	4.07942	4.08544	0.147
91	4.03760	4.03141	0.154	4.11408	4.10575	0.203
92	4.07137	4.07176	0.010	4.15105	4.14854	0.061
93	4.08673	4.08572	0.025	4.16596	4.16925	0.079
94	4.11792	4.11397	0.096	4.19784	4.19441	0.082
95	4.12896	4.13582	0.166	4.20427	4.21294	0.206
96	4.14529	4.15212	0.164	4.22149	4.22953	0.190
97	4.15242	4.15367	0.030	4.23333	4.23415	0.019
98	4.17297	4.17074	0.053	4.24888	4.24690	0.047
99	4.18994	4.18888	0.025	4.27899	4.27740	0.037
100	4.20373	4.21285	0.216	4.28904	4.29176	0.064
101	4.22958	4.23006	0.011	4.30977	4.31112	0.031
102	4.24199	4.24296	0.023	4.32438	4.32504	0.015
103	4.25360	4.25075	0.067	4.33687	4.33486	0.046
104	4.28642	4.28345	0.069	4.36950	4.36567	0.088
105	4.30657	4.30624	0.008	4.39228	4.39207	0.005
106	4.31547	4.31995	0.104	4.40638	4.40694	0.013
107	4.34118	4.34193	0.017	4.42091	4.42370	0.063
108	4.34935	4.35598	0.152	4.43621	4.44172	0.124
109	4.36295	4.36176	0.027	4.44922	4.44494	0.096
110	4.37974	4.37984	0.002	4.46691	4.46202	0.110
111	4.39652	4.38614	0.237	4.47881	4.46618	0.283
112	4.40482	4.41073	0.134	4.48982	4.49513	0.118
113	4.42003	4.41888	0.026	4.49809	4.50730	0.204
114	4.42672	4.42968	0.067	4.51862	4.51611	0.055
115	4.44940	4.46193	0.281	4.53519	4.54067	0.121
116	4.46937	4.47430	0.110	4.55608	4.55307	0.066
117	4.48235	4.48380	0.032	4.56374	4.56785	0.090
118	4.50482	4.50569	0.019	4.59148	4.59609	0.100
119	4.50733	4.51327	0.132	4.59729	4.60078	0.076
120	4.52413	4.52782	0.081	4.60960	4.61562	0.131
121	4.53911	4.54276	0.080	4.62762	4.63458	0.150
122	4.56333	4.56602	0.059	4.64820	4.65923	0.237
123	4.57367	4.57286	0.018	4.66121	4.66642	0.112
124	4.60540	4.60303	0.051	4.69278	4.69228	0.011
125	4.61532	4.62032	0.108	4.70740	4.71043	0.064
126	4.62818	4.62519	0.065	4.71517	4.71609	0.020
127	4.63514	4.63026	0.105	4.72725	4.71991	0.155
128	4.64194	4.64199	0.001	4.73331	4.73754	0.089
129	4.66690	4.66430	0.056	4.75924	4.75618	0.064
130	4.66790	4.66597	0.041	4.76674	4.75845	0.174
131	4.69246	4.68730	0.110	4.78743	4.78038	0.147
132	4.70527	4.71080	0.118	4.80128	4.80542	0.086
133	4.72046	4.73008	0.203	4.81305	4.82061	0.157
134	4.75051	4.75395	0.072	4.84664	4.84559	0.022
135	4.75900	4.76169	0.057	4.85021	4.85330	0.064
136	4.76976	4.77384	0.085	4.86402	4.86321	0.017
137	4.77918	4.77950	0.007	4.87531	4.87473	0.012
138	4.79086	4.79493	0.085	4.88149	4.88582	0.089
139	4.80450	4.80244	0.043	4.89785	4.89637	0.030
140	4.81875	4.81484	0.081	4.91309	4.90863	0.091
141				4.93822	4.94346	0.106
142				4.95627	4.95918	0.059

Table 6 continued on next page.

Table 6 continued.

Index	300 K			4 K		
	f_{exp} (MHz)	f_{calc} (MHz)	diff (%)	f_{exp} (MHz)	f_{calc} (MHz)	diff (%)
143				4.96168	4.96342	0.035
144				4.98300	4.98143	0.032
145				4.98846	4.99420	0.115
146				4.99438	5.00516	0.215
147				5.01215	5.01596	0.076
148				5.02882	5.03051	0.034
149				5.04591	5.05275	0.135
150				5.06142	5.06270	0.025